

See discussions, stats, and author profiles for this publication at: <https://www.researchgate.net/publication/317019283>

SEISMIC CHARACTERIZATION of FAULT FACIES MODELS

Article in *Interpretation* · May 2017

DOI: 10.1190/int-2016-0226.1

CITATIONS

9

READS

515

5 authors, including:



Charlotte Botter

University of Leeds

17 PUBLICATIONS 140 CITATIONS

[SEE PROFILE](#)



Nestor Cardozo

University of Stavanger (UiS)

73 PUBLICATIONS 1,783 CITATIONS

[SEE PROFILE](#)



Dongfang Qu

University of Copenhagen

21 PUBLICATIONS 69 CITATIONS

[SEE PROFILE](#)



Jan Tveranger

Norce Research

161 PUBLICATIONS 1,256 CITATIONS

[SEE PROFILE](#)

Some of the authors of this publication are also working on these related projects:



Seismic Imaging of Fault Zones [View project](#)



Digital Rock Physics [View project](#)

Seismic characterization of fault facies models

Charlotte Botter¹, Nestor Cardozo², Dongfang Qu³, Jan Tveranger³, and Dmitriy Kolyukhin⁴

Abstract

Faults play a key role in reservoirs by enhancing or restricting fluid flow. A fault zone can be divided into a fault core that accommodates most of the displacement and a surrounding damage zone. Interpretation of seismic data is a key method for studying subsurface features, but the internal structure and properties of fault zones are often at the limit of seismic resolution. We have investigated the seismic response of a vertical fault zone model in sandstone, populated with fault facies based on deformation band distributions. Deformation bands reduce the porosity of the sandstone, and they condition its elastic properties. We generate synthetic seismic cubes of the fault facies model for several wave frequencies and under realistic conditions of reservoir burial and seismic acquisition. Seismic image quality and fault zone definition are highly dependent on wave frequency. At a low wave frequency (e.g., 10 Hz), the fault zone is broader and no information about its fault facies distribution can be extracted. At higher wave frequencies (e.g., 30 and 60 Hz), seismic attributes, such as tensor and envelope, can be used to characterize the fault volume and its internal structure. Based on these attributes, we can subdivide the fault zone into several seismic facies from the core to the damage zone. Statistical analyses indicate a correlation between the seismic attributes and the fault internal structure, although seismic facies, due to their coarser resolution, cannot be matched to individual fault facies. The seismic facies can be used as input for reservoir models as spatial conditioning parameters for fault facies distributions inside the fault zone. However, relying only on the information provided by seismic analyses might not be enough to create high-resolution fault reservoir models.

Introduction

Fault zones are routinely interpreted as 2D surfaces in seismic data, although they are actually narrow volumes of deformed rock with petrophysical properties differing from the surrounding host rock (Faulkner et al., 2010). The rock volume affected by fault deformation, or the fault zone, can be subdivided into a fault core of varying thickness, accommodating most of the displacement, and a surrounding damage zone (Caine et al., 1996; Wibberley et al., 2008). Fault deformation decreases more or less in a systematic manner from a maximum at the center of the fault to zero at the fault damage zone boundary (e.g., Rotevatn et al., 2007; Brogi, 2008; Schueller et al., 2013). In highly porous sandstone reservoirs, the damage zone can be composed of deformation bands, which are millimeter to centimeter thick zones of localized compaction, formed by disaggregation or cataclasis (e.g., Antonellini and Aydin, 1994; Fossen et al., 2007). Cataclastic deformation bands are usually associated with a reduction in porosity, permeability,

and fluid flow (e.g., Antonellini and Aydin, 1994; Fossen and Bale, 2007; Fossen et al., 2007; Rotevatn et al., 2007; Torabi et al., 2013).

Despite the impact of faults on reservoir connectivity, standard industrial modeling tools still lack methods and workflows allowing realistic representation of fault zones in reservoir models (Tveranger et al., 2005; Braathen et al., 2009; Manzocchi et al., 2010). This is due to the fact that faults are usually represented as single surfaces with a transmissibility parameter (Manzocchi et al., 2010; Pei et al., 2015), and it is also because there are no standard quantitative and systematic methods to describe fault zones in 3D at reservoir scales (e.g., Braathen et al., 2009; Pei et al., 2015). Recent studies have demonstrated the feasibility of including fault zones into reservoir models using a combination of volumetric fault zone grids and fault facies (e.g., Tveranger et al., 2005; Fredman et al., 2007, 2008; Braathen et al., 2009; Fachri et al., 2011, 2013a, 2013b, 2016; Qu and Tveranger, 2016). In porous sandstones, deformation bands can be

¹Formerly University of Stavanger, Department of Petroleum Engineering, Stavanger, Norway; presently Dublin Institute for Advanced Studies (DIAS), School of Cosmic Physics, Geophysics Section, Dublin, Ireland. E-mail: charlotte.botter@gmail.com; cbotter@cp.dias.ie; nestor.cardozo@uis.no.

²University of Stavanger, Department of Petroleum Engineering, Stavanger, Norway. E-mail: nestor.cardozo@uis.no.

³UniResearch CIPR, Bergen, Norway. E-mail: qudongfang2012@gmail.com; jan.tveranger@uni.no.

⁴Trofimuk Institute of Petroleum Geology and Geophysics, Novosibirsk, Russia. E-mail: kolyukhindr@ipgg.sbras.ru.

Manuscript received by the Editor 6 December 2016; revised manuscript received 7 March 2017; published ahead of production 16 May 2017. This paper appears in *Interpretation*, Vol. 5, No. 4 (November 2017); p. 1–18, 12 FIGS., 2 TABLES.

<http://dx.doi.org/10.1190/INT-2016-0226.1>. © 2017 Society of Exploration Geophysicists and American Association of Petroleum Geologists. All rights reserved.

quantified and subdivided into classes, i.e., fault facies, according to their density (Fachri et al., 2011, 2013a, 2013b, 2016; Qu and Tveranger, 2016). Most previous models using fault facies (e.g., Syversveen et al., 2006; Fredman et al., 2007, 2008; Soleng et al., 2007; Fachri et al., 2011, 2013a, 2013b) have been limited by the size of the high-resolution grid needed to represent fault heterogeneities. Qu et al. (2015, 2017), Qu and Tveranger (2016), and Fachri et al. (2016) incorporate these high-resolution fault facies models into larger scale reservoir models and perform fluid flow simulations. Their studies confirm the importance of taking into account the 3D structure of faults and their internal properties for planning the production of hydrocarbon fields.

Faults zones are difficult to image on seismic because they are often at the limit of seismic resolution (e.g., Townsend et al., 1998; Dutzer et al., 2010; Long and Imber, 2010). The number of studies that investigate the potential of seismic data to characterize fault zone architecture and properties (e.g., Townsend et al., 1998; Koledoye et al., 2003; Cohen and Coult, 2006; Long and Imber, 2010, 2012; Hale, 2013; Botter et al., 2014, 2016, 2017) has increased during the past few years. Many of these studies include the use of seismic attribute-based workflows. Dutzer et al. (2010) estimate fault architecture and fault sealing by using a combination of semblance, dip, and tensor attributes. Iacopini and Butler (2011) and Iacopini et al. (2012) use opacity, structurally oriented filters, volume attributes, and other image processing and visualization techniques to improve imaging of a deepwater fold and thrust belt. Iacopini et al. (2016) apply tensor, semblance, and instantaneous phase attributes to define unsupervised seismic facies from fault zones. Botter et al. (2016, 2017) use a combination of semblance, tensor, and/or dip attributes to extract fault geobodies from 3D synthetic seismic images of normal faulting and of an outcrop-based relay ramp model. Torabi et al. (2016a, 2016b) use a series of coherence and filtered coherence attributes to quantify the relation between fault displacement and fault length along strike. The outcomes of these studies clearly show the importance and viability of interpreting faults as volumes as well as single planes.

Internal fault structure and properties are, however, at the limit of, if not less than, seismic resolution. For typical depths of investigation of 2–4 km, seismic will hardly capture vertical features measuring less than 12–25 m. The horizontal resolution, which is crucial for evaluating 3D fault architecture, is highly dependent on many factors, including noise, seismic acquisition design, and equipment used. Uncertainties in the horizontal resolution are larger than the vertical ones, often by a factor of two (Sheriff and Geldart, 1995). Moreover, prior to interpretation, the seismic data may have gone through several processing steps that may influence the seismic image. It is therefore reasonable to question to what extent the impact of fault-related deformation is captured in seismic images. Deformation bands in porous sandstone reservoirs are subseismic features

that cannot individually be imaged or interpreted on seismic. In fault zones, deformation bands are normally densely spaced or form clusters (e.g., Fossen et al., 2007; Schueller et al., 2013), which affect bulk petrophysical properties including elastic impedance. This in turn influences seismic response. Botter et al. (2017) show that a fault damage zone composed of deformation bands in an otherwise homogeneous sandstone reservoir can be imaged on synthetic seismic. They also show that when the reservoir model is subjected to fluid flow during production, the deformation bands do not have a strong influence on seismic response, and cannot be imaged or interpreted anymore. When looking at the seismic response of deformation bands integrated into a high-resolution fault facies grid (e.g., Qu and Tveranger, 2016), we will face similar issues regarding the impact of deformation band properties on seismic amplitude. Therefore, we may ask the following questions: Is it possible to extract information about fault facies from seismic data? How dependent is the seismic response on seismic acquisition and processing parameters? Furthermore, is it possible to relate seismic attributes to the distribution of fault facies in the fault zone?

To address these questions, this paper investigates the seismic response of a reservoir-scale fault-zone model populated with fault facies based on an empirical distribution model for deformation bands in fault zones (Qu and Tveranger, 2016). We use a synthetic workflow combining an ultra-high resolution fault model with fault facies, forward seismic modeling, attribute-based interpretation, and quantitative/statistical analyses for integration into the reservoir model (Figure 1). The input model (Qu and Tveranger, 2016) consists of a vertical kilometer size, ellipsoidal normal fault zone with 100 m maximum displacement (Figure 1a). The fault-zone grid is populated using four fault facies representing different frequencies of deformation bands (Figure 1b, fault facies: U_{FF} = undeformed, L_{FF} = low deformation, M_{FF} = medium deformation, and H_{FF} = high deformation). The facies definitions and their spatial distribution patterns are based on statistics derived from outcrop studies (Schueller et al., 2013). The initial porosity of the sandstone and the porosity changes induced by the different deformation band densities are used to condition the rock elastic properties. Using a ray-based prestack depth migration (PSDM) simulator (Lecomte, 2008; Lecomte et al., 2015), we generate synthetic seismic cubes under realistic conditions of seismic acquisition and reservoir burial, for several wave frequencies (Figure 1c). Seismic image quality and fault damage zone definition are highly dependent on the wave frequency. Seismic attributes, such as the tensor (a measure of the dominant reflector's direction) and the signal envelope (a measure of the instantaneous magnitude of the trace), can be fine-tuned to characterize the fault volume. A combination of these attributes helps to subdivide the fault zone in several seismic facies from core (high deformation) to damage zone

(lower deformation) (Figure 1d, seismic facies: U_{SF} , undeformed; L_{SF} , low deformation; M_{SF} , medium deformation; and H_{SF} , high deformation). Statistical analyses confirm a correlation between the seismic attributes and the fault internal structure, although it is not possible to retrieve the high-resolution fault facies distribution directly from the seismic data. However, the seismic facies obtained by the seismic attribute analysis can be used as spatial conditioning parameters for fault facies-based reservoir modeling (Figure 1e).

Methodology

Fault facies model

This paper uses a fault facies model described by Qu and Tveranger (2016) from which the essential is summarized here. The input to the fault facies model setup consists of statistics derived from empirical data including detailed outcrop maps, scanlines of deformation band density, petrophysical properties of deformation bands, and distribution of displacement. The damage zone around the normal fault is modeled vertically as an ellipsoid with 100 m maximum displacement at its center and zero at its edges (Figure 1a). The dimensions of the fault-zone grid are (x or fault-dip direction, y or fault-strike direction, and z or depth) = $100 \times 1200 \times 600$ m, with a resolution (x, y, z) of $1 \times 5 \times 5$ m. The width of the fault zone is defined using a scaling relationship between the damage zone width and the fault throw (Schueller et al., 2013). The facies definitions and their spatial distribution patterns are based on statistics derived from multiple outcrop studies (Schueller et al., 2013). The definition of individual fault facies is linked to the deformation band density at the scale of the grid resolution: $>20/\text{m}$ (high or H_{FF}), $6\text{--}20/\text{m}$ (medium or M_{FF}), $1\text{--}5/\text{m}$ (low or L_{FF}), and $0/\text{m}$ (undeformed or U_{FF}) (Figure 1b). The spatial distribution of these fault facies inside the fault zone is modeled based on the likelihood of occurrence of each pattern relative to each other, using truncated Gaussian simulation (Fachri et al., 2013a, 2013b; Qu and Tveranger, 2016). The key input parameters of the model are facies proportion trends and variogram ranges.

The initial porosity of the sandstone is assumed to be 25% (Qu and Tveranger, 2016). Cataclastic deformation bands have a negative impact on porosity (e.g., Antonellini and Aydin, 1994; Rotevatn et al., 2007; Torabi et al., 2013). Here, the deformation band porosity is set to 5% (Aydin, 1978; Antonellini and Aydin, 1994; Qu and Tveranger, 2016). To estimate the impact of deformation bands on porosity, the porosity in each cell (ϕ_{cell}) is computed using an arithmetic average based on the volume of deformation bands per cell and the remaining volume of host sandstone (Qu and Tveranger, 2016; Botter et al., 2017):

$$\phi_{\text{cell}} = \frac{V_{\text{ss}} \times \phi_{\text{ss}} + V_{\text{DBs}} \times \phi_{\text{DB}}}{V_{\text{total}}}, \quad (1)$$

where V_{ss} is the volume of sandstone, ϕ_{ss} is the initial porosity of the sandstone (0.25), V_{DBs} is the volume of

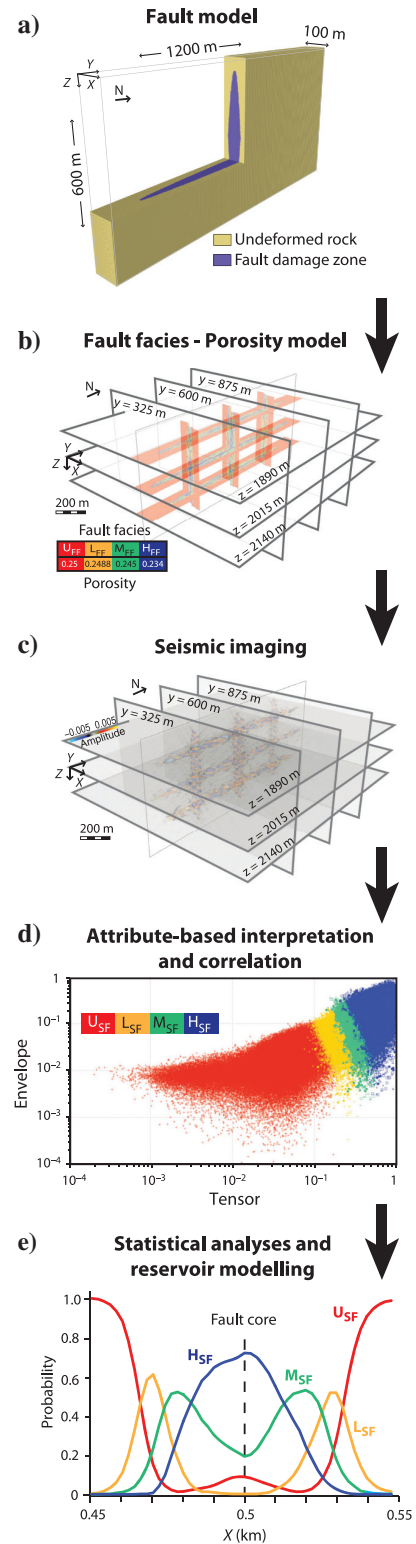


Figure 1. Workflow of this study: (a) input vertical fault zone model, (b) fault facies model with porosity distribution (fault facies: U_{FF} , undeformed; L_{FF} , low deformation; M_{FF} , medium deformation; and H_{FF} , high deformation), (c) synthetic seismic cube for a 60 Hz wave frequency, (d) attribute analysis and correlations (seismic facies: U_{SF} , undeformed; L_{SF} , low deformation; M_{SF} , medium deformation; and H_{SF} , high deformation), and (e) statistical analyses and input probability trends for reservoir modeling.

deformation bands (for each fault facies), ϕ_{DB} is the porosity of deformation bands (0.05), and V_{total} is the volume of the cell. As we do not distinguish the total from the effective porosity and as porosity is a scalar, this arithmetic average gives a good estimation of the porosity changes.

Computation of elastic properties

The definition of elastic parameters, i.e., P- and S-wave velocities (V_P , V_S) and density ρ , is necessary to obtain the reflectivity for seismic modeling. The only property we use from the fault facies model is porosity. The elastic properties are computed using existing rock-physics models for high-porosity sandstone. The Gassmann (1951) theory is a reasonable model for such reservoirs (Mavko et al., 2009). To use Gassmann's equations in our model, we consider the sandstone reservoir as homogeneous and isotropic and the pore space as connected. Thus, the deformation bands are taken into account only by their impact on the reservoir porosity. Gassmann's equation uses the porosity of the rock and the bulk and shear moduli of the rock and fluids in place. Standard values for the bulk and shear moduli for sandstone and brine water are used. Combined with the porosity and water saturation, we can compute V_P , V_S , and ρ by applying the Reuss mixture model (Mavko et al., 2009).

Simulation of seismic imaging

For seismic modeling, we use a ray-based 3D PSDM simulator (Lecomte, 2008), which is a fast, user-oriented, and accurate tool for synthetic seismic imaging of geologic models (Lecomte et al., 2015, 2016). This simulator handles diffracted energy, such as that resulting from faults or other discontinuities. It also deals with 3D effects in resolution and illumination as func-

tion of various parameters, such as survey geometry, overburden, burial depth, and wavelet (Figure 2).

A complete description of the technique is given by Lecomte (2008), and its direct application to geologic modeling of faults is given by Botter et al. (2014, 2016, 2017), Lecomte et al. (2015, 2016), and Wood et al. (2015). The structural input to the PSDM simulator is an incident-angle-dependent reflectivity grid obtained from the elastic properties, V_P , V_S , and ρ (Figure 2a). In the wavenumber domain, ray-based modeling is used to generate PSDM filters that are dependent on the survey geometry, frequency content, wave type, and velocity model (Figure 2b). The reflectivity grid is converted to the wavenumber domain by a fast Fourier transform (FFT) and then multiplied by the PSDM filter. The final simulated seismic image in the spatial domain is obtained by applying an inverse FFT to this product (Figure 2c). The PSDM filter can be converted by applying an inverse FFT to a point-spread function (PSF), which is the point-scatter response of the PSDM filter (Figure 2d). The entire imaging process in the wavenumber domain is equivalent to a 3D convolution of the reflectivity grid with the PSF in the spatial domain (Figure 2c and 2d).

Seismic attribute-based interpretation

Once 3D seismic cubes are obtained, we can apply seismic attribute-based automated techniques to improve the definition of the fault zone and its internal structure. Iacopini and Butler (2011), Iacopini et al. (2016), and Botter et al. (2016) describe the seismic attributes for fault characterization. Two seismic attributes are considered in this study: the tensor and the signal envelope, or reflection strength.

The tensor attribute is based on a structurally oriented tensor. The algorithm produces a symmetric ten-

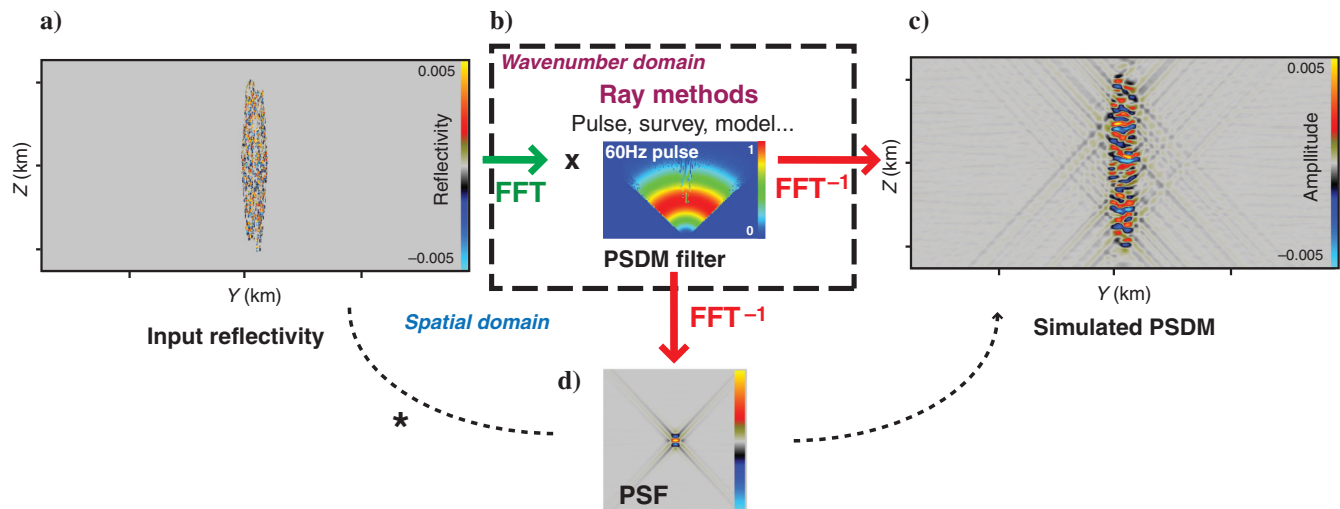


Figure 2. The PSDM simulator. (a) A reflectivity grid is input in the spatial domain. This input reflectivity is converted to the wavenumber domain using an FFT. (b) Ray methods are used to calculate a PSDM filter in the wavenumber domain. (c) The product of the PSDM filter and the input reflectivity in the wavenumber domain, plus an inverse FFT (FFT⁻¹) on the result of this operation produces the simulated PSDM image. (d) The entire process is equivalent to the convolution of the PSF with the input reflectivity in the spatial domain.

sor, whose principal axes define the local reflector's orientation (Gersztenkorn and Marfurt, 1999). The attribute is a combination of the three eigenvalues of the tensor and identifies reflector discontinuities. This attribute is sensitive to amplitude changes and has the potential to highlight fault damage consisting of deformation band clusters (Botter et al., 2017). The signal envelope attribute represents the instantaneous energy of the signal, and it is proportional in magnitude to the reflection coefficient (Taner et al., 1979). It has a low-frequency appearance, only positive amplitudes, and good horizontal resolution. It often highlights key seismic features, such as discontinuities, changes in lithology, and faults. By merging the two attributes into one cube, we can combine both effects to enhance the response of the damage zone. A fault enhancement filter can be applied to the cube of the two combined attributes to improve continuity along the fault zone. This filter can be used as an expression of confidence level of having a fault. Its size allows the definition of larger or smaller fault features, which could help to target seismic facies on the attribute cube.

Statistical analysis

Statistical analysis can be used to retrieve the input fault facies distribution and properties from seismic data and/or seismic attributes and facilitate comparison between these. As a first statistical approach, correlation coefficients between the input rock property, i.e., porosity, and the seismic attributes can be computed. The Pearson's linear correlation coefficient r_{UV} between two parameters U and V is calculated as follows (Hald, 1952):

$$r_{UV} = \frac{\sum_{i=1}^N (U_i - \bar{U})(V_i - \bar{V})}{\sqrt{\sum_{i=1}^N (U_i - \bar{U})^2 \sum_{i=1}^N (V_i - \bar{V})^2}}, \quad (2)$$

where \bar{U} and \bar{V} are the sample means. Here, U is the porosity and V is the seismic attribute, and the correlation coefficient is the spatial averaging for the studied domain, i.e., the fault zone. We also apply a t -test to test the significance of the correlation coefficient ($r_{UV} \neq 0$) and to reject the null hypothesis. The null hypothesis is defined such as there is no correlation between porosity and the seismic attribute. This null hypothesis is rejected if the following inequality is satisfied (Hald, 1952):

$$\left| \frac{r_{UV} \sqrt{N-2}}{\sqrt{1-r_{UV}^2}} \right| \geq t(N-2, \alpha), \quad (3)$$

where N is the overall sample size and α is the significance level, here set at 5% according to normal statistical usage. If the null hypothesis is rejected, there is a correlation between the porosity and the seismic attribute, and variogram ranges of the attribute are calculated. A variogram describes the geometry and the continuity of a variable (Gringarten and Deutsch, 2001), and it is a way to express the ranges of definition of heterogeneities, or in our case fault facies. Here, we try to find a correspon-

dence between the properties of the original fault facies model and the properties extracted from the seismic attributes. The computed variogram of the seismic attribute can be compared with the variogram of the fault facies model. The fault facies model is simulated as a random field (Qu and Tveranger, 2016). Because the simulated seismic images are highly heterogeneous, we also treat the seismic attributes as random fields. We remove the mean trend of the seismic attribute and transform it to a statistically homogeneous random field using the variogram for a normalized function:

$$\tilde{F}(X) = \frac{F(X) - E\{F(X)\}}{\sqrt{\text{Var}\{F(X)\}}}. \quad (4)$$

In this study, we deal with only one realization of the fault-zone model. Therefore, the mean value and the variance spatial distribution are estimated using a moving average (Hadley, 1969). This technique is commonly used in time series analysis to reduce the impact of fluctuations and determine long-term trends. The variogram of a random function \tilde{F} is described by the following equation (Cressie, 1991):

$$2\gamma(h) = \text{Var}\{\tilde{F}(X) - \tilde{F}(Y)\} = E\{(\tilde{F}(X) - \tilde{F}(Y))^2\}, \quad (5)$$

where X and Y are the coordinate vectors defining the spatial position of two points in the fault zone, h is the distance between X and Y , E is the mathematical expectation, Var is the variance, and the semivariogram $\gamma(X, Y)$ is one half of the variogram $2\gamma(X, Y)$. After removing the mean trend in equation 4, and assuming a constant mean, we can apply the variogram estimator based on the method of moments (Cressie, 1991):

$$2\hat{\gamma}(h) = \frac{1}{N(h)} \sum_{N(h)} (\tilde{F}(X_i) - \tilde{F}(X_j))^2, \quad (6)$$

where $N(h)$ is the number of pairs of points X_i and X_j located at a distance h from each other. Note that variogram sill estimates produced in this manner are sensitive to the size of the moving averaging estimate, but the technique can nevertheless be used to estimate variogram ranges.

Results

Fault facies model properties

As an input for our workflow (Figure 1b), we use one realization of a fault facies model using a spherical variogram model setup with a range of 2 m in the x -direction and 50 m in the y - and z -directions. The porosity of the undeformed host-rock sandstone, corresponding to the U_{FF} facies, is 25% (Figure 1a and 1b). The other fault facies all represent deformed rock with reduced porosity values. Porosity reaches a minimum value of 23.4% in the H_{FF} fault facies; having the highest frequency of deformation bands (Figure 3a and Table 1). This gives a porosity contrast of 6.4% between the undeformed and most deformed rock. Figure 3a shows that most of the H_{FF} , or facies with 23.4% porosity,

is located toward the center of the fault zone and exhibits a more continuous distribution parallel to the fault. This is in small part due to the cell dimensions ($x, y, z = 1 \times 5 \times 5$ m), but mainly to the fact that deformation bands are continuous in length and depth and line up parallel to the fault (e.g., Fossen et al., 2007).

The computation of the elastic properties (V_P , V_S , and ρ) is based on porosity only, and it considers a brine-saturated model. The distribution of elastic properties within the fault zone therefore correlates directly with the porosity distribution (Figure 3a). Where the porosity decreases, V_P , V_S , and ρ increase. The actual values are displayed in Table 1. Seismic response results from contrasts in elastic properties; therefore, only their relative changes are of interest. A porosity contrast of only 6%, as in this case, is difficult to detect on seismic images. However, because the fault zone is within homogeneous sandstone, we can illuminate it if the seismic resolution allows it.

Seismic images

The elastic properties are used to compute an incident-angle reflectivity cube (Figure 3b), which is the input for the PSDM simulator. To avoid boundary effects and to match the reservoir model size of Qu and Tver-

anger (2016), we create a grid populated with a reflectivity parameter of $(x, y, z) = 1000 \times 1000 \times 600$ m and a resolution of $(x, y, z) = 1 \times 5 \times 5$ m. The grid encompasses the area of elastic property variations. The continuous distribution of the high H_{FF} or medium M_{FF} fault facies in the y - and z -directions (Figure 3a) corresponds to a reflectivity of zero (Figure 3b). The reflectivity shows subseismic features corresponding to the fault facies adjacent contacts that will generate diffractions.

Several simulation constraints need to be defined to obtain seismic images representative of reservoir conditions. We first translate the model to 2 km depth, which is the depth used in the fluid-flow simulation by Qu and Tveranger (2016). Representative values for average velocities and density for high-porosity sandstone at this depth are $V_P = 2770$ m/s and $\rho = 2100$ kg/m³ (Mavko et al., 2009). We define a layered overburden composed of an interbedded succession of four layers of shale and sandstone (Figure 4). Starting from a sea-bottom depth of 500 m (seawater; Batzle and Wang, 1992), the elastic properties increase down to the target depth (Figure 4; Mavko et al. [2009], for sandstone; and Horsrud et al. [1998], and Nygård et al. [2006], for shale). A simulated marine survey is centered above the model with 25 shot lines and eight north-oriented (parallel to y and the fault strike) streamers fully covering the model area. We use three zero-phase Ricker pulses of 60, 30, and 10 Hz. A wave frequency of 60 Hz is unlikely to be retrieved at the depth of consideration. It can however help to highlight the subseismic fault features displayed on the reflectivity grid. For all the synthetic seismic cubes, the amplitude has been calibrated such that a reflectivity of intensity one corresponds to an amplitude value of one on the seismic image.

Figure 5 shows the results of the PSDM simulation for three crosslines at $y = 875$ m (first row), $y = 600$ m (second row), and $y = 325$ m (third row), and the three wave frequencies (see the crossline locations in Figure 1b and 1c). The corresponding fault facies

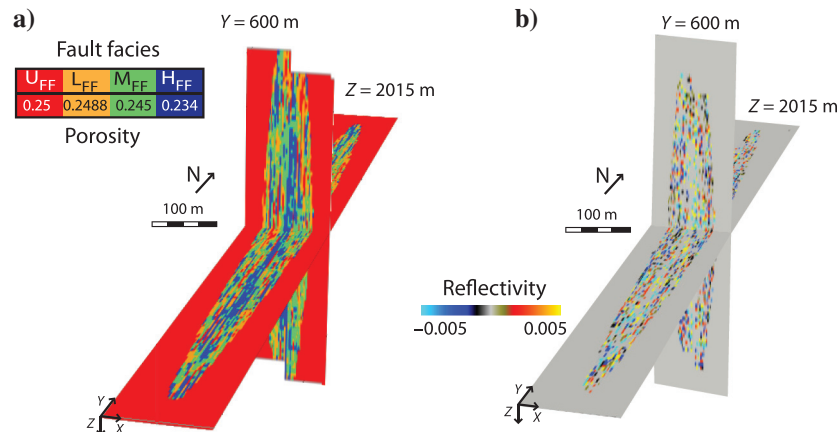


Figure 3. (a) Fault facies and porosity distribution in the fault damage zone and (b) the corresponding reflectivity based on the elastic-property computations.

Table 1. Rock properties associated with each fault facies (U_{FF} , undeformed; L_{FF} , low; M_{FF} , medium; and H_{FF} , high). The maximum changes in properties are indicated at the bottom.

Fault facies	Porosity	V_P (m/s)	V_S (m/s)	Density (kg/m ³)
U_{FF}	0.2500	2848.3	1684.5	2202.5
L_{FF}	0.2488	2852.1	1686.8	2204.6
M_{FF}	0.2450	2862.4	1692.7	2210.4
H_{FF}	0.234	2899.8	1713.9	2331.1
	Max decrease		Max increase	
	6.4%	1.80%	1.75%	1.30%

sections are displayed in Figure 5a. At high frequency (60 Hz, Figure 5b), the horizontal and vertical resolutions are very good (respectively 12 and 25 m, see PSF). On the crosslines, diffractions are visible within and at the boundary of the fault zone. Some horizontal reflection events are also visible inside the fault zone, and they correspond mainly to the vertical contrast between fault facies (Figure 5a). Small displacements can be spotted in the middle and southern sections (Figure 5b, second and third rows), and they fit the vertical features of H_{FF} (Figure 5a). At this level of resolution, it is possible to interpret the fault zone as an ellipsoid, even though the fault facies distribution is not directly interpretable. At 30 Hz (Figure 5c), the resolution is lower (50 m in the x -direction and 25 m in depth).

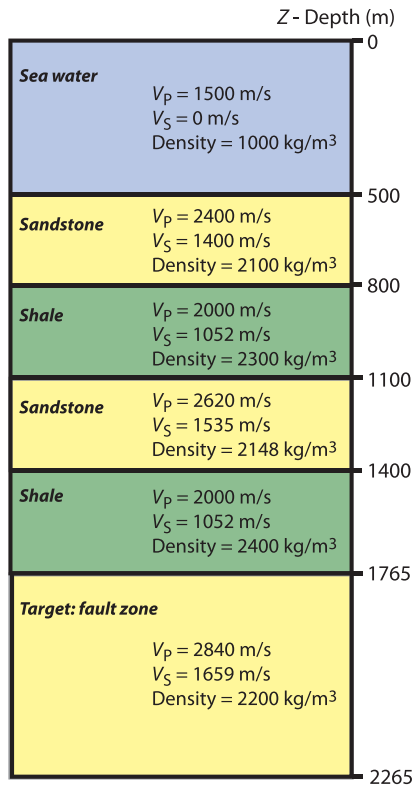


Figure 4. Overburden used in the PSDM simulation showing the rock properties for each sandstone and shale layer from an assumed sea bottom at 500 m depth to the target depth of the fault model between 1765 and 2265 m.

Although the fault zone is mainly characterized by diffractions, it is still possible to interpret its border and its internal heterogeneous distribution of properties. The correspondence to the input fault facies distribution (Figure 5a) is, however, less obvious. At low frequencies (10 Hz, Figure 5d), the fault has almost no impact on the seismic image. Indeed, the horizontal resolution is more than 100 m (the entire fault is below the seismic resolution), such that only diffractions are visible at the location of the fault. Crosslines do not allow identifying vertical displacement within the fault zone at any wave frequency (overlay of fault displacement in Figure 5d).

Depth slices can improve the definition of the fault zone and its internal property distribution. Figure 6 presents slices at three depths for the fault facies distribution (Figure 6a), and the three wave frequencies (Figure 6b–6d; see Figure 1b–1c for the location). The three depth slices at 60 Hz (Figure 6b) define the ellipsoidal shape of the damage zone very well. The internal part of the fault is characterized by high amplitude values, but not-clear reflective events can be interpreted or related to the fault facies. The fault zone is mainly defined by diffractions that are still visible away from the damage zone boundaries. At 30 Hz (Figure 6c), the fault zone presents lower amplitude values and less diffractions. The PSF shows that the internal architecture of the fault is at the limit of the seismic resolution in the x - and y -directions. At 10 Hz (Figure 6d), the fault zone is below the seismic resolution, showing only some diffractions.

Wave frequency has a strong impact on the seismic image of the fault zone. The higher the frequency, the

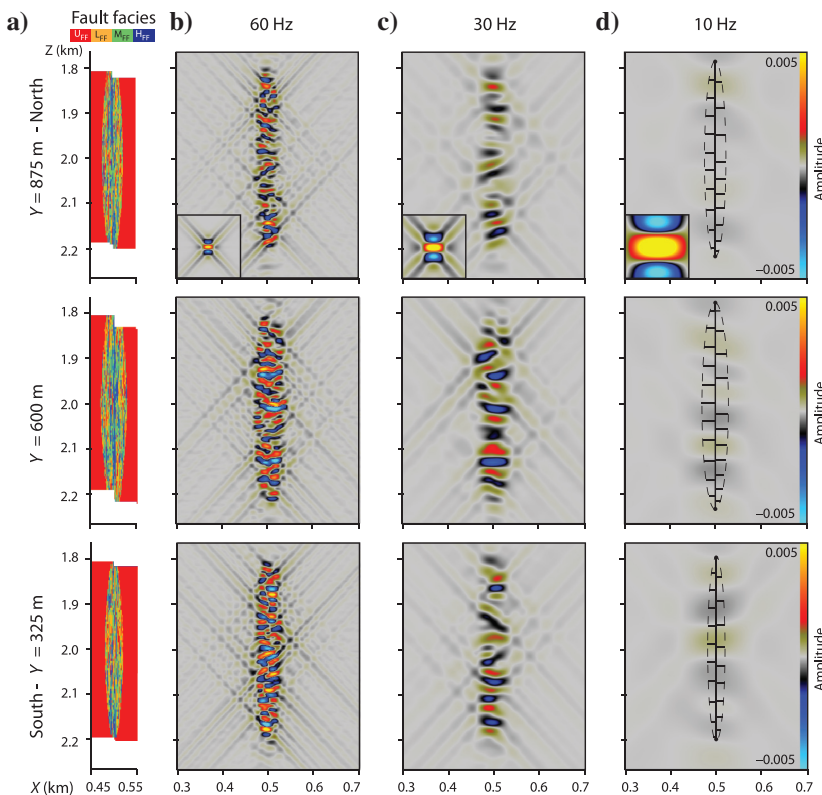


Figure 5. (a) Fault facies and seismic sections at $y = 875$ m (first row), $y = 600$ m (second row), and $y = 325$ m (third row) for three wave frequencies: (b) 60, (c) 30, and (d) 10 Hz. The PSFs in cross-sectional view are displayed on the bottom left corner of each seismic image in the first column. The ellipsoidal shape of the damage zone and the vertical displacement profile are also displayed in (d). The locations of the crosslines are indicated in Figure 1b and 1c.

better the ellipsoidal shape of the fault zone stands out. Although some elements of the internal structure of the fault can be distinguished on the 60 Hz seismic cube (Figures 5b and 6b), there are hardly any similar patterns visible on the 30 Hz images (Figures 5c and 6c). At 10 Hz, the fault has almost no impact on the seismic image and cannot be interpreted.

Attribute-based description of the fault zone

Although the seismic image by itself is insufficient to interpret the damage zone, especially at low frequen-

cies, a suitable combination of seismic attributes could improve the interpretation. Figure 7 presents one cross-line at $y = 600$ m (center of the fault with the maximum displacement) for the three wave frequencies. When comparing directly the seismic section (Figure 7a) with the corresponding input fault facies section (Figure 7b), it is clear that there is no direct correlation between the fault facies distribution and the seismic response. The horizontal resolution is not good enough, even at 60 Hz, to see lateral changes of fault facies. Using the tensor

attribute improves the vertical continuity of the fault

features at 60 Hz (Figure 7c, first row).

Indeed, although the seismic image displays mostly horizontal reflection events, the high values of the tensor attribute display vertical features. The tensor attribute, however, displays a fault zone that is thinner than the input model, and the distribution of attribute values does not directly match the fault facies distribution. The envelope attribute shows a good definition of the ellipsoidal shape of the fault. It highlights mainly the diffractive events, showing more localized patches of high values (Figure 7d, first row). The fault enhancement filter is applied to the combination of the tensor and envelope attributes. As expected, high values of fault enhancement are concentrated in an ellipsoidal shape corresponding to the fault zone. The highest values are toward the center or core of the fault (Figure 7e, first row). At 30 Hz, the tensor attribute still displays an ellipsoidal fault zone, although it shows less vertical continuity than the 60 Hz cube because there are less amplitude changes in the 30 Hz seismic cube (Figure 7c, second row). The envelope attribute shows a more irregular shape of the fault zone and highlights more vertical features than in the 60 Hz cube (Figure 7d, second row). The fault enhancement filter really helps to define the fault and its internal structure. The highest values of fault enhancement (Figure 7e, second row) are similarly distributed as the H_{FF} in the input model (Figure 7b). At 10 Hz, the envelope attribute renders a better definition of the fault zone than the tensor attribute (Figure 7c and 7d, third row). Hence, the fault enhancement filter shows high values matching mainly the envelope attribute (Figure 7e, third row). Due to the low seismic resolution, the fault zone is interpreted as a larger area than at 30 and 60 Hz, and less information from the internal part is visible.

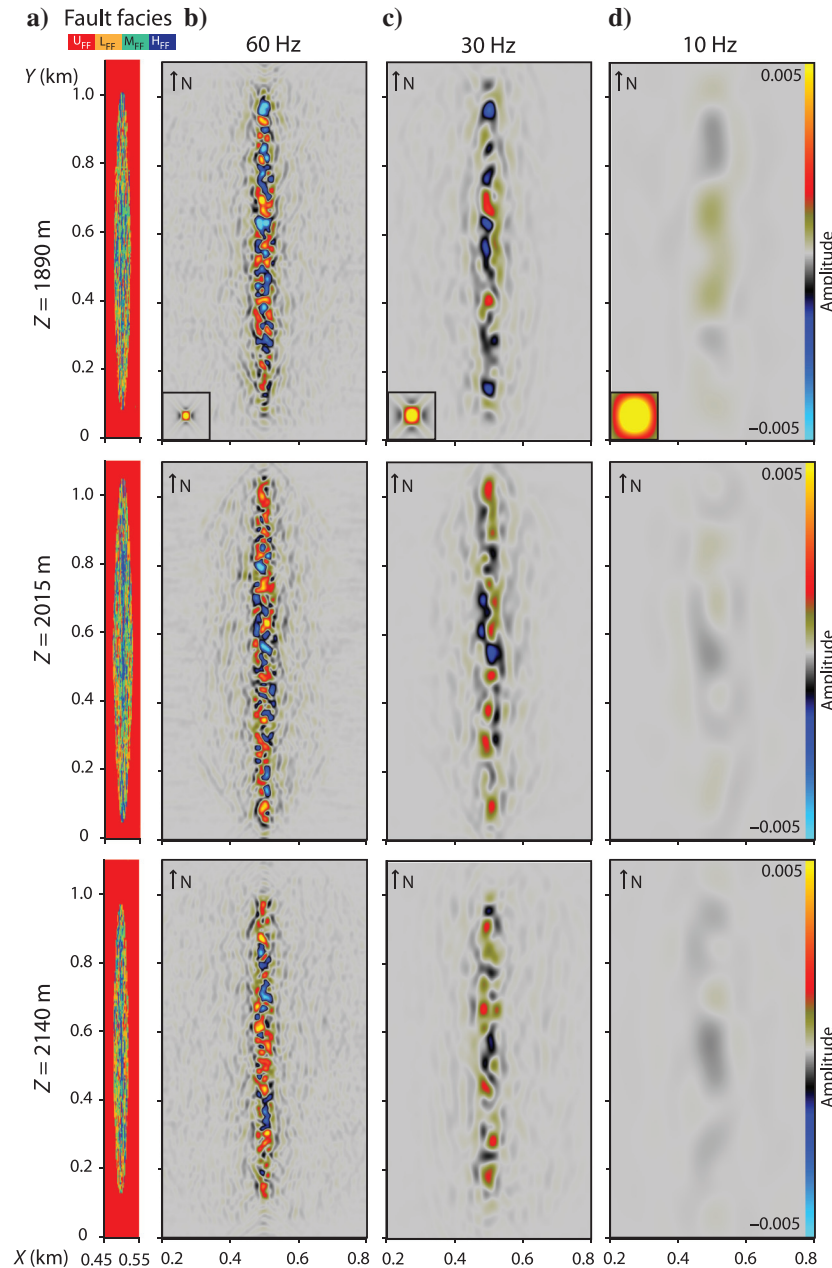


Figure 6. (a) Fault facies and seismic depth slices at $z = 1890$ m (first row), $z = 2015$ m (second row), and $z = 2140$ m (third row) for three wave frequencies: (b) 60, (c) 30, and (d) 10 Hz. The PSFs in cross-sectional view are displayed on the bottom left corner of each seismic image in the first column. The locations of the depth slices are indicated in Figure 1b and 1c.

The tensor and envelope attributes do not exhibit any continuity along the y -axis on depth slices (Figure 8c and 8d), as does the H_{FF} fault facies (Figure 8b). At 60 Hz, the tensor attribute shows better results than the envelope attribute (Figure 8c and 8d, first row). The fault enhancement filter provides a better definition of the fault zone and continuity along strike (Figure 8e, first row). At 30 Hz, the fault enhancement on the tensor and envelope attributes yields to an improved rendering of the fault, even though it does not visually match the fault facies distribution (Figure 8b–8d, second row). At 10 Hz, the envelope attribute defines better the shape of the fault than the tensor, and the fault enhancement again mainly matches the envelope attribute (Figure 8c–8e, third row).

A qualitative study of seismic attributes helps to define the overall fault shape. The choice of tensor and

envelope helps to strengthen the fault zone shape from high to low frequencies. However, even with the use of seismic attributes, we still are not able to extract much information about the internal structure of the fault and its facies distribution.

Seismic facies analysis

To explore in a more quantitative way the seismic attributes, we compute the correlation coefficient between the input porosity distribution and the tensor and envelope attributes (equation 2; Table 2). This analysis is run on a grid sample with dimensions matching the input fault facies model ($x, y, z = 100 \times 1200 \times 600$ m). The t -test described in equation 3 shows that in all cases the null hypothesis (that there is no correlation between the porosity and the seismic attribute) is rejected. Therefore, we can use the correlation coefficient for further

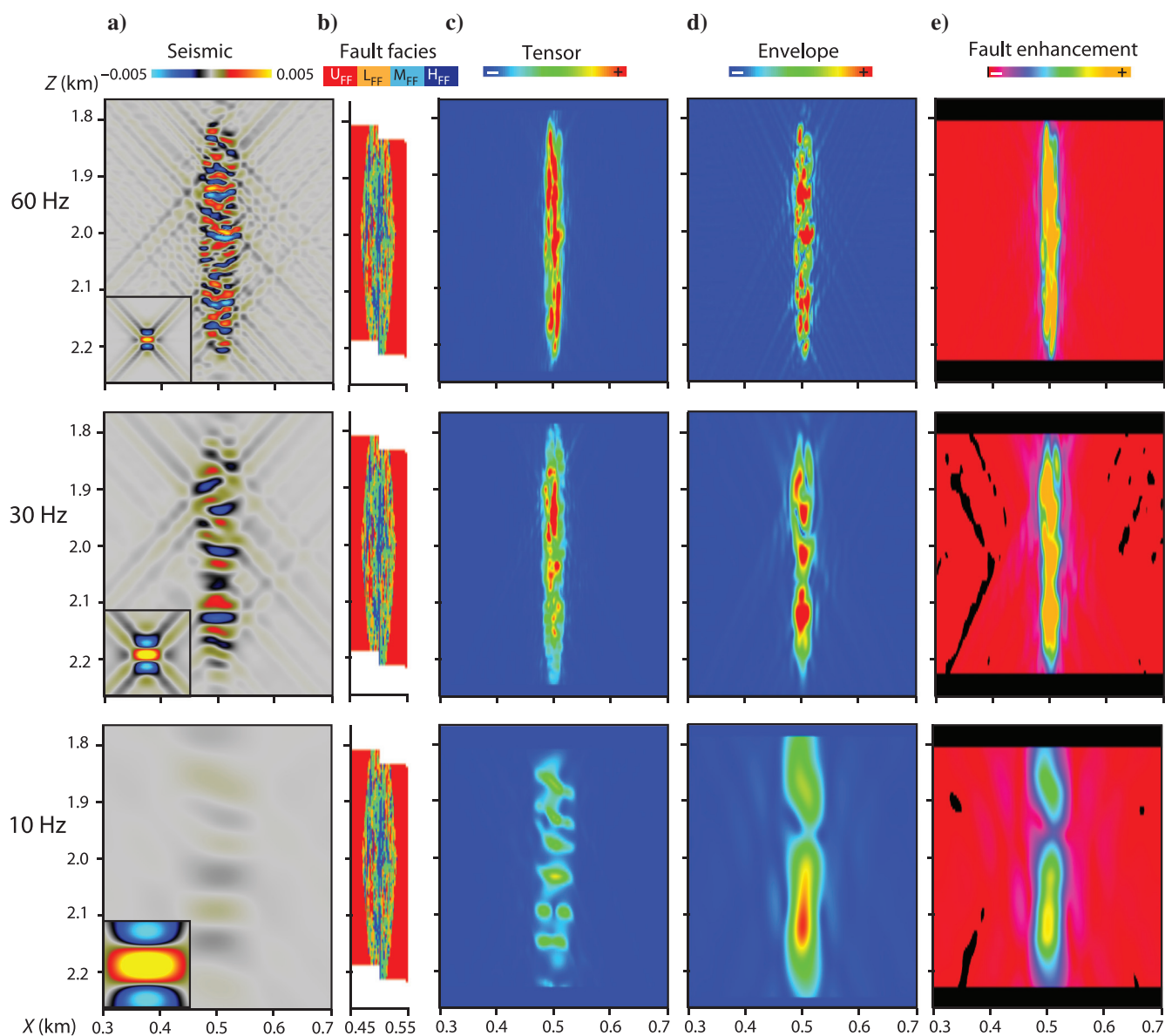


Figure 7. Crossline at $y = 600$ m showing (a) the seismic for the three wave frequencies (rows), (b) the input fault facies model, (c) the tensor and (d) envelope attributes, and (e) the fault enhancement filter applied to the combination of tensor and envelope.

analyses. There is a negative correlation between the porosity and the seismic attributes, meaning that the tensor and envelope values increase, whereas porosity

decreases. The tensor and envelope are correlated to the porosity for the three wave frequencies. The absolute value of the correlation factor decreases with wave

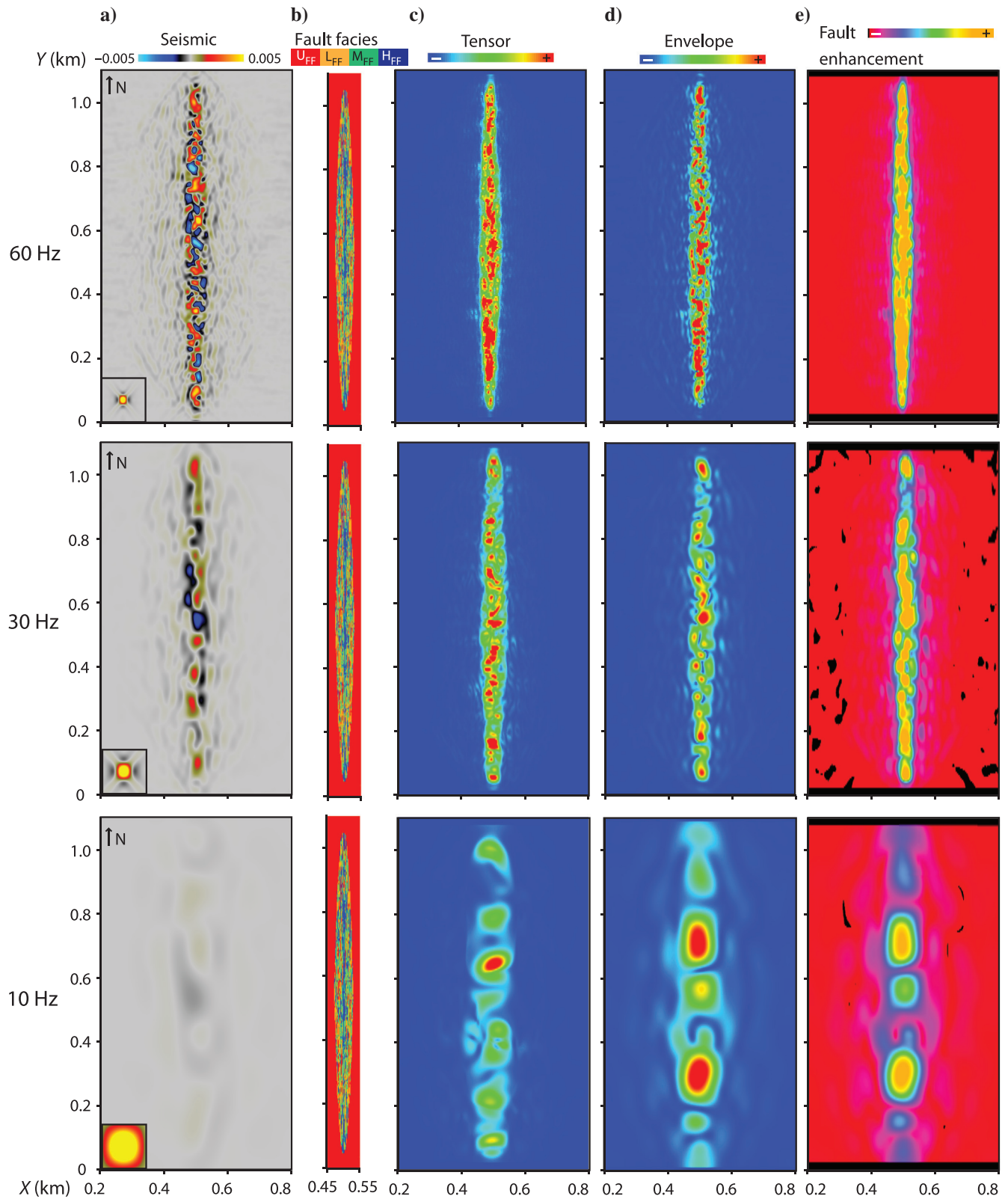


Figure 8. Depth slice at $z = 2015$ m showing (a) the seismic for the three wave frequencies (rows), (b) the input fault facies model, (c) the tensor and (d) envelope attributes, and (e) the fault enhancement filter applied to the combination of tensor and envelope.

frequency. The correlation coefficients show that the tensor attribute has a better correlation with porosity at higher frequencies (60 and 30 Hz), whereas the envelope attribute is better correlated at 10 Hz. The best correlation coefficient is actually between the porosity and the fault enhancement filters (Table 2), thus highlighting that the combination of seismic attributes improves the definition of the fault zone.

As a first step to relate the seismic image to the input fault facies, we plot the tensor versus the envelope attributes for the three wave frequencies (Figure 9a). The dots are color coded by the corresponding input fault facies. With a logarithmic scale, it is easy to locate the undeformed fault facies (U_{FF}) or host rock in red for all wave frequencies. The upper limit of U_{FF} corresponds to values between 0.1 and 0.2 for the tensor and envelope attributes. However, for all wave frequencies, the low (L_{FF}), medium (M_{FF}), and high (H_{FF}) deformation fault facies are all superimposed for high values of the tensor and envelope attributes. Therefore, it is difficult to separate the H_{FF} from the M_{FF} or the L_{FF} facies, even though the higher the fault deformation, the higher the attribute values. Figure 9a shows that the definition of the fault zone by the tensor attribute decreases with wave frequency (lower values and density of points), whereas for the envelope attribute it increases with wave frequency (higher values and larger density of points). Although the attributes improve the definition of the fault zone, even at low frequencies, crossplotting them does not reveal any specific trend or group of fault facies. Is it still possible to extract some information about fault facies from the seismic?

Figure 9b shows the same plots of tensor versus envelope attribute, but this time the dots are color coded according to the fault enhancement filter. The higher values of this filter correspond to higher confidence of having a fault, which can be interpreted as higher values of deformation. We divide the color scale in four classes, with respect to the distribution of fault enhancement values for each frequency. These four-color classes are equivalent to seismic facies from the crossplots of the attributes at the three wave frequencies. Seismic facies are 3D mappable units based on properties derived from seismic amplitude, frequency, velocity, etc. (e.g., Mitchum et al., 1977; Dumay and Fournier, 1988). Because no well data are available for calibration, these groups are unsupervised seismic facies. The low values of fault enhancement can be defined as the undeformed seismic facies (U_{SF}). This U_{SF} (Figure 9b) displays a very good match with the fault facies

U_{FF} (Figure 9a), especially at 60 and 30 Hz. The boundaries of this facies are, however, harder to identify at 10 Hz (Figure 9b, third row). The other seismic facies, e.g., low (L_{SF}), medium (M_{SF}), and high (H_{SF}), distributed linearly along the axes of the tensor and envelope attributes. This seismic facies distribution (Figure 9b) does not match the input fault facies distribution at any wave frequency (Figure 9a), but it gives an overview of the deformation within the fault zone.

To further exploit these seismic facies, we can extract seismic volumes, or geobodies corresponding to each seismic facies. Figure 10 shows the geobodies corresponding to the four seismic facies at the three wave frequencies. At 60 Hz (Figure 10a), the seismic facies iso-

Table 2. Correlation coefficients between the porosity and the selected seismic attributes at the three wave frequencies.

Wave frequency (Hz)	Tensor attribute	Envelope attribute	Fault enhancement filter
60	-0.564	-0.497	-0.589
30	-0.467	-0.427	-0.503
10	-0.204	-0.267	-0.283

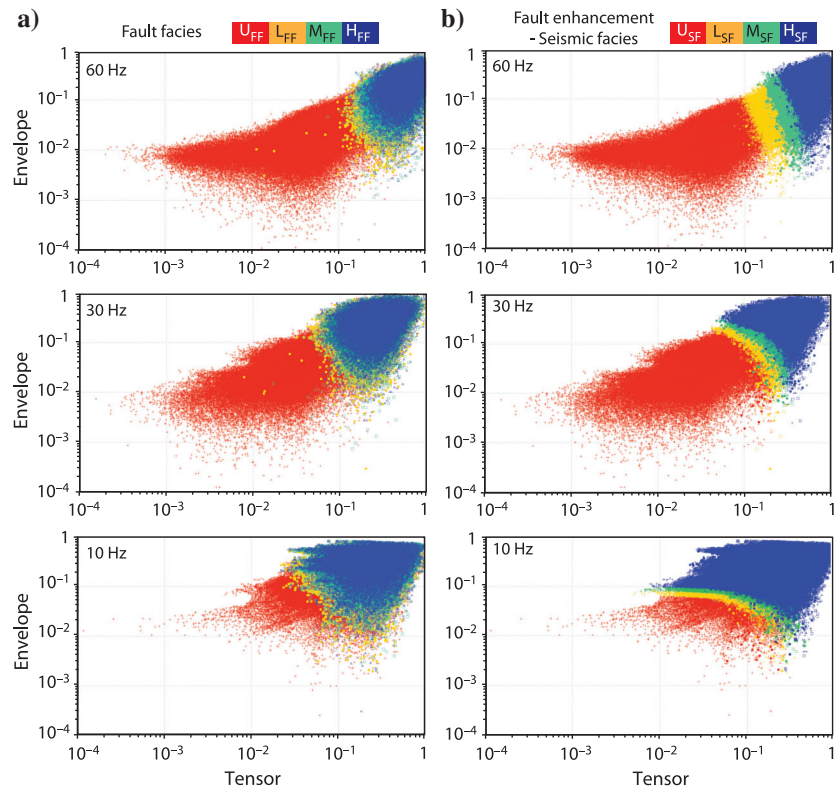


Figure 9. Crossplots of the tensor versus envelope attributes for the three wave frequencies (rows). The attribute values have been normalized from 0 to 1 and are displayed with a logarithmic scale. (a) The dots are color coded according to the four fault facies (FF), and (b) according to four classes of the fault enhancement filter. These four classes are referred as seismic facies (SF).

lates the fault zone as an ellipsoid. The U_{SF60} shows the entire external model including the host rock. The L_{SF60} is an outer envelope of deformed rock. The M_{SF60} forms an internal envelope closer to the fault core. The H_{SF60} represents the central part of the fault, including the fault core. This volume has a maximum thickness of 50 m. The seismic facies at 30 Hz (Figure 10b) show similar patterns, from the entire model, to more internal envelopes, and to the core. The ellipsoidal shape of the central area, H_{SF30} , is not as uniform as for the 60 Hz cube and has a maximum thickness of 60 m. The seismic facies for the 10 Hz cube (Figure 10c) are much wider and more irregularly shaped than those at higher frequencies. However, it is possible to distinguish the different envelopes from no deformation (U_{SF10}) to high deformation (H_{SF10}). The proportion of the less deformed facies (U_{SF10} , L_{SF10}) is smaller than the proportions of more highly deformed facies (M_{SF10} , H_{SF10}). The H_{SF10} has a maximum thickness of 100 m. By displaying the seismic facies from low deformation to high deformation, we are able to estimate the distribution of the deformation within the fault zone based only on seismic data and attribute-analyses, even at low wave frequency.

Seismic facies as input for reservoir modeling

To populate the reservoir grid representing the fault zone, we need to define facies probability trends in 3D and variogram ranges. Qu and Tveranger (2016) use facies probability trends based on a large outcrop collection of deformation band densities in high-porosity sandstone. The four fault facies trends corresponding to the U_{FF} , L_{FF} , M_{FF} , and H_{FF} facies for ranges $z = [1870-2129]$ m and $y = [375-830]$ m are shown in Figure 11a. The H_{FF} has a higher probability to occur next to the fault core and a lower probability to occur near the fault zone boundary. The M_{FF} and L_{FF} facies have less probability to be in the fault core. The probability of these facies is maximal just outside the fault core and decreases toward the fault zone boundary. The probability of U_{FF} increases away from the fault core.

We could also use the information provided by the seismic facies to condition the spatial distribution of the fault facies. To do that, we use the seismic facies at several wave frequencies of Figure 10 to create facies probability trends. The derived probabilities are shown in Figure 11b–11d. At 60 Hz (Figure 11b), the seismic facies trends have overall similar probability distributions as the outcrop-based fault facies trends (Fig-

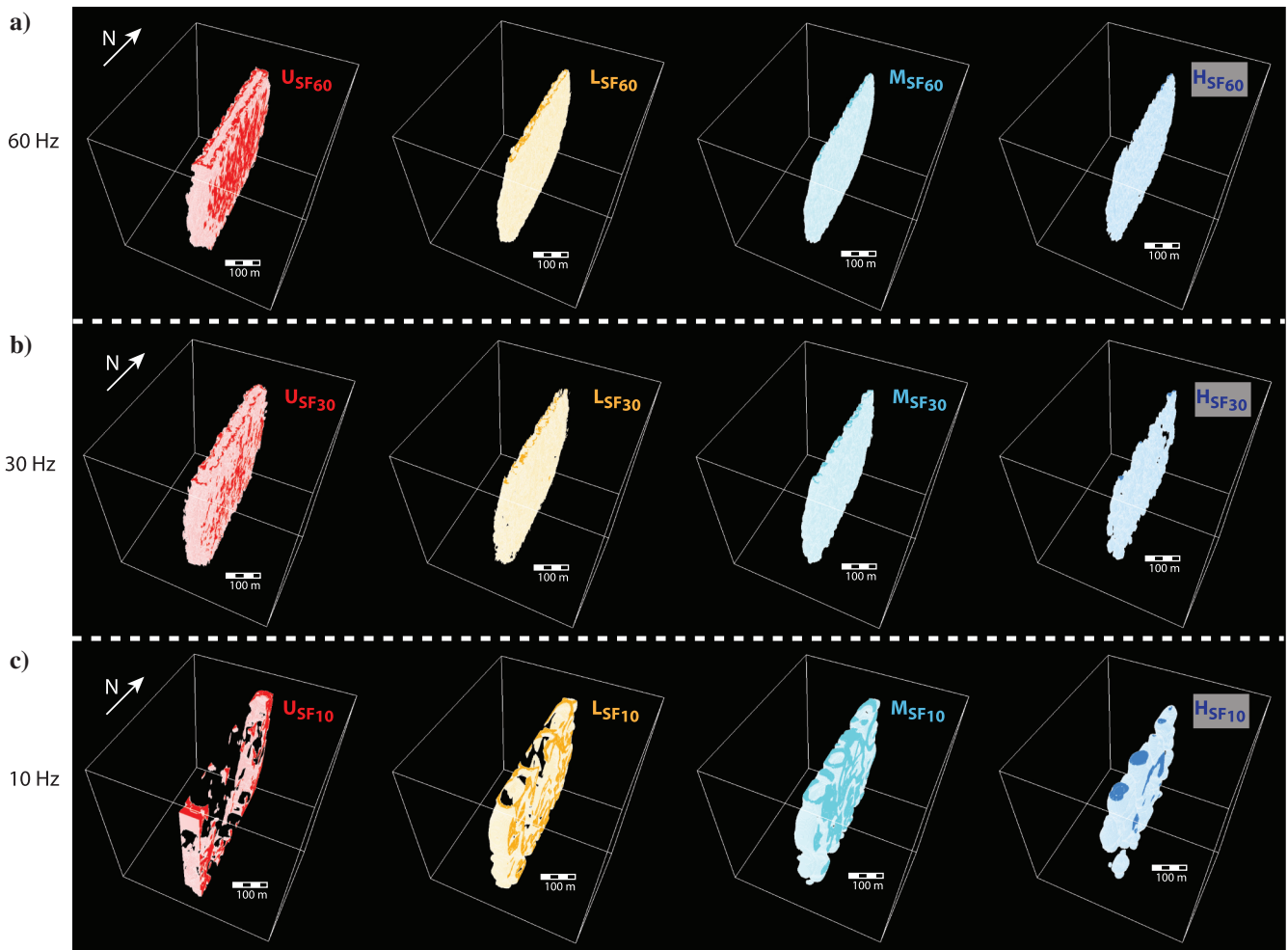


Figure 10. Volumes showing the four seismic facies (columns) for the three waves frequencies: (a) 60, (b) 30, and (c) 10 Hz.

ure 11a). However, the distribution along the x -axis of the seismic facies is wider than the corresponding input fault facies (Figure 11a and 11b). The accuracy of the seismic facies probability trends relative to those from the outcrop data decreases with lower wave frequencies (Figure 11c and 11d). At 10 Hz (Figure 11d), the trends for the M_{SF10} and L_{SF10} seismic facies have almost the same probability across the fault zone.

The second input for stochastic modeling of the fault zone is spherical variogram ranges. Qu and Tveranger (2016) use ranges of $(x, y, z) = 2 \times 50 \times 50$ m based on the cell sizes and accuracy obtained from the outcrop database. We compute variograms based on the fault enhancement filter for the three wave frequencies (Figure 12). For the spherical variograms, the ranges can be visually interpreted by picking the lag where the sill is reached. From Figure 12, we can estimate that the variogram ranges in the x - (Figure 12a) and z - (Figure 12b) directions for 60 Hz are approximately 15–25 and 35–40 m, respectively. Thus, through seismic attribute analysis, we can define large variogram ranges, but there are limitations for small variogram range estimation. From the seismic data, it is not possible to obtain a variogram range of 2 m in the x (fault dip)-direction as in the input fault facies model. Furthermore, decreasing wave frequencies lead to lower correlation coefficients between porosity and seismic attributes (Table 2), and lower resolution in the variogram estimation (Figure 12). With a 100 m wide fault zone model, it is not possible to obtain variogram ranges in the x -direction for the 30 and 10 Hz seismic cubes (Figure 12a). Indeed, to obtain the variogram ranges in the x -direction at these frequencies, we would need a larger sample grid in this direction. In the z (vertical)-direction, the depth of the model is large enough to estimate a variogram range of 45–50 m for the 30 Hz cube, and 60–80 m for the 10 Hz cube (Figure 12b). Therefore, only high-resolution seismic data can be used as stand-alones to estimate variogram ranges. When dealing with fault zones at the limit or below seismic resolution, we would need extra information, such as well data, to define the variogram ranges for the faults.

Discussion

We have investigated the seismic response of a sandstone reservoir model with a vertical normal fault damage zone populated using fault facies techniques. The workflow used here (Figure 1) takes as input a fault facies model from

Qu and Tveranger (2016). The model is populated with a set of four fault facies defined by different deformation band densities. The spatial distribution and extent of these facies is well-constrained in the x (fault dip)-direction. However, there are large uncertainties in the other directions, partly due to the limited availability of 3D outcrop data (Qu and Tveranger, 2016). Deformation bands reduce the permeability and porosity of the host sandstone, hence the fluid flow. The integration of a high-resolution fault facies grid into a reservoir model does affect the fluid flow (Fachri et al., 2016; Qu and Tveranger, 2016; Qu et al., 2017). If the fault zone properties influence petrophysical properties and fluid flow, they can also impact the seismic response (e.g., Fossen and Bale, 2007; Botter et al., 2017). The computation of elastic properties in the sandstone relies on variations in its porosity due to deformation bands. Their relative changes in this case are however less than 6%, which are rather low. Botter et al.

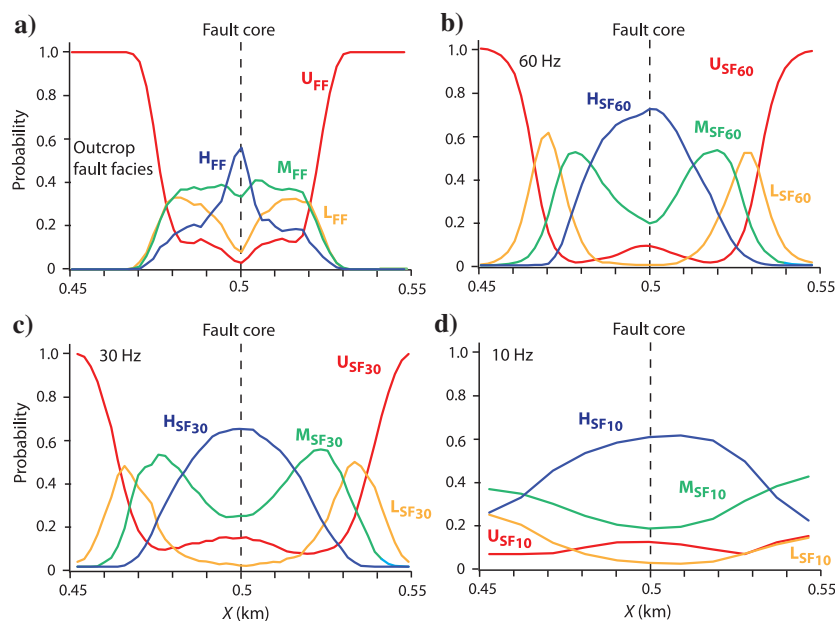


Figure 11. Facies probability trends along the fault-dip direction averaged for $z = [1870\text{--}2129]$ m and $y = [375\text{--}830]$ m. (a) The four fault facies probability trends used for the input model. The four seismic facies probability trends computed from the (b) 60, (c) 30, and (d) 10 Hz seismic cubes.

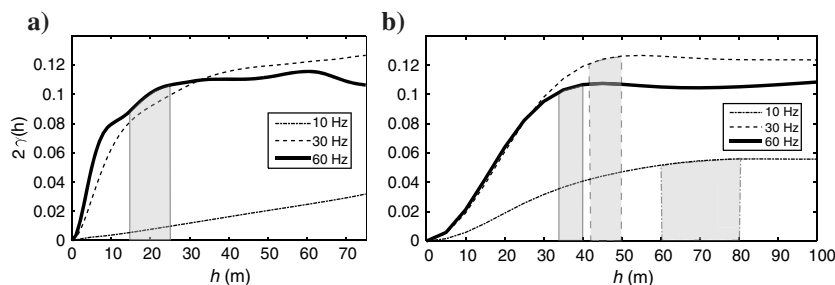


Figure 12. Variograms along the (a) x - (fault dip), and (b) z (vertical)-directions for the three wave frequencies. The shaded areas correspond to the approximate variogram ranges for each wave frequency. Note that along the x -direction, (a) the grid dimensions do not allow to obtain the ranges for the 30 and 10 Hz seismic cubes.

(2017) show that a change in elastic properties twice that amount would completely be masked on seismic images with fluid contacts. This effect would be even more accentuated if the input model were a different fault facies realization with weaker adjacent elastic contrasts. The fault zone is within a homogeneous sandstone reservoir, and therefore the small changes in porosity and elastic properties between fault facies can still be imaged. However, the internal structure of the fault zone would most probably be masked if it were within a more complex layered stratigraphic sequence of, e.g., sandstone and shale.

Fault architecture also plays an important role on the resultant seismic image. The fault is modeled using a very high-resolution grid. The meter cell size highlights subseismic features, even though it is already an up-scaled version of the outcrop database. However, the rectangular shape of the cells and the fault facies is not entirely realistic and can affect the seismic response. Indeed, with the settings used for seismic imaging, we illuminate mainly horizontal features. Because the fault zone and the internal fault facies distribution are modeled vertically, the seismic response is mostly at the top and corners of the rectangular cells, where diffractions are generated. A fault with a lower dip angle of, e.g., 45° would probably give better results because the fault-parallel fabric would be much more able to generate a seismic response. Modeling such fault geometry will be the subject of future work.

The PSDM simulator provides an efficient way to investigate the impact of realistic acquisition parameters, and reservoir and depth conditions on the resultant seismic images of the fault zone. The simulator is more advanced than the standard 1D convolution used in industry, and although it does not provide the complete modeling of methods solving the full-wave equation (e.g., finite-difference techniques), it handles 3D effects in resolution and illumination, which are essential for imaging the fault facies model (Lecomte, 2008; Lecomte et al., 2015, 2016). By modeling PSDM images, we target the best processing of seismic data for imaging discontinuities, such as faults. The simulator provides noise-free images; therefore, our seismic interpretation is only dependent on the fault internal structure and seismic resolution. The PSDM simulator can handle the complexity of a fault facies model (Lecomte et al., 2015), but the final seismic image relies on the reflectivity grid, i.e., the contrast in elastic properties and their distribution within the fault zone, and the acquisition settings. Seismic resolution is investigated for several wave frequencies. At low frequency (i.e., 10 Hz), it is almost impossible to define accurately the fault shape and location, and even less the internal fault facies distribution. The 60 Hz wave frequency at 2 km depth is unlikely to be retrieved. However, synthetic seismic at such high frequencies can provide details for the interpretation of faults at shallower depths. Seismic images at 60 Hz show a very good vertical resolution, even though the horizontal resolution in the x and y does not capture the distribution of fault facies. At 30 Hz, a typical wave frequency at reservoir

depths, the information provided by the seismic images is enough to identify a fault zone. One has to be aware though that the fault damage might be masked in real seismic data, e.g., due to noise, or if the fault were put in a more complex stratigraphic succession.

Seismic attributes help to improve the definition of the fault zone at any wave frequency. However, before applying seismic attributes, one should be aware of the conditions of seismic acquisition and processing, and the fault features to be enhanced (Taner, 2001; Chopra and Marfurt, 2005, 2007; Marfurt and Alves, 2015). Most seismic attributes have been developed for poststack seismic data (Chopra and Marfurt, 2005), i.e., seismic data that exhibit the same reflection character as that of a single source-receiver pair with no offset. The PSDM simulator allows us to use a 0° incident angle cube. Therefore, our attribute analyses can be extrapolated to fault characterization in poststack seismic data. The choice and tuning of the tensor and envelope attributes have been calibrated by sensitivity analyses related to the distribution of facies within the fault zone. The tensor attribute is sensitive to changes in amplitude and reflector orientations (Gersztenkorn and Marfurt, 1999). On the 60 Hz seismic cube, the amplitude values are relatively high within the fault zone, showing some reflection events (Figure 5b). The horizontal resolution along the fault-dip direction is not good enough to separate vertical features, but the tensor is able to highlight the most important fault facies boundaries (Figure 7a). Moreover, there is a strong negative correlation between the tensor and the input porosity. Therefore, the tensor has a strong potential for internal characterization of the fault model. The signal-envelope attribute is a trace-based attribute that is proportional to the acoustic impedance or reflection strength (Chopra and Marfurt, 2005). In our seismic images, it mainly highlights the diffraction from the fault zone, which can be useful to characterize subseismic features, such as fault facies (Figure 5). At low frequency (10 Hz), the amplitude values are too low to show any reflection. However, the envelope attribute substantially enhances the definition of the fault zone boundary and overall variation of internal properties (Figures 7d and 8d). The correlation coefficient between the envelope and input porosity is also higher at low frequencies. Based on the selection of attributes and our statistical analyses, a combination of the tensor and the envelope attributes can highlight several aspects of the fault internal structure. However, crossplots of tensor versus envelope attributes do not help to retrieve directly the input fault facies distribution. Iacopini et al. (2016) use a crosscorrelation of dip versus semblance attributes to define thrust-related features and separate faulting from other disturbances in the seismic data. In our disturbance-free seismic cubes, we can easily separate the host rock corresponding to the lowest values of the tensor and envelope attributes, especially at 60 and 30 Hz (Figure 9). However, even knowing the host-rock properties and how they are affected by faulting, we are still not

able to use directly the attribute crossplots to interpret in detail the internal fault facies distribution.

Seismic facies studies often rely on the appropriate combination of seismic attributes, which can be calibrated with well data to retrieve petrophysical properties. Seismic facies recognition is widely applied within stratigraphic interpretation of depositional environments, sediment source, and lithofacies (e.g., Vail, 1987). Iacopini et al. (2016) use the correlation of attributes to perform unsupervised, i.e., without well-data calibration, seismic facies classification. After defining a geobody of the seismic fault damage zone corresponding to low values of tensor attributes, they use crossplots of attributes within the geobody to define facies related to the fault zone and not to noise artifacts. In our seismic attribute analysis, we use the fault enhancement filter for unsupervised seismic facies classification. By tuning the window of calculation of this filter, we can target larger or smaller features. The fault enhancement filter applied to a combination of the tensor and envelope attributes shows the best correlation coefficient with the porosity grid for all wave frequencies (Table 2). Therefore, using fault enhancement on the combination of attributes is the best option for seismic interpretation of the fault facies. We go a bit further than Iacopini et al. (2016) by defining our seismic facies as a representation of fault deformation. Indeed, previous studies on synthetic data show that the fault enhancement filter can be used for characterization of fault deformation. Botter et al. (2016) show crossplots of seismic amplitude versus volumetric and shear strain, where the high values of fault enhancement correspond to high strains. Botter et al. (2017) use an appropriate tuning of tensor and semblance attributes and the fault enhancement filter to separate faulting from fluid contacts in a reservoir model of a relay ramp. The seismic facies distribution here relates to the general observation that a fault core accumulates most of the deformation, and that the deformation decreases toward the damage-zone boundaries (e.g., Caine et al., 1996; Rotevatn et al., 2007; Brogi, 2008). Our study also shows that defining the seismic facies based on the tensor versus envelope crossplot is quite subjective (Figure 9b). The four seismic facies are based on our input model with four fault facies. Defining the undeformed facies U_{SF} for all wave frequencies can be done by choosing a value of 0.1–0.2 for normalized scales of tensor and envelope. However, the higher deformation facies, L_{SF} , M_{SF} , and H_{SF} , vary with wave frequency, and defining their limits using attributes values is not straightforward, especially at low frequencies. Therefore, the number of facies has to be adjusted as function of the quality of the data and the information available on rock properties. Moreover, the cell size of our fault grid is ultrafine, but if the cells are larger than $1 \times 5 \times 5$ m, one might restrict the interpretation to two or three seismic facies.

The ultimate purpose of interpreting seismic data is to create geo and reservoir models. To do that, we use the seismic facies as input for probability trends modeling, and we compute variogram ranges based on the seismic

attributes. Therefore, even if our seismic-based probability trends are more approximate than the outcrop-based probability trends (Figure 11), they represent direct 3D observations of specific subsurface fault zone properties, which may not be provided by the outcrop data, and can be used to condition specific stochastic fault zone models. The choice of a spherical variogram is meant to fit the fault facies modeling of Qu and Tveranger (2016). They use a spherical variogram model with ranges of 2 m in the x -direction and 50 m in the y - and z -directions, which is a first approximation of the fault facies spatial direction. Our results show that one of the main limitations of the seismic attribute analysis is that it is not possible to estimate short length variogram ranges in the x (fault dip)-direction matching those of the input fault facies model (Figure 12). This was also observed by the statistical analysis of Vishnevsky et al. (2014) and Kolyukhin et al. (2015) on synthetic seismic images modeled using a standard finite-difference scheme (Virieux, 1986; Lisitsa et al., 2010; Vishnevsky et al., 2014). Moreover, to obtain the variogram ranges, the sample size matters. In our case, we are not able to obtain variogram ranges in the x -direction for the 30 and 10 Hz when considering a 100 m wide fault zone. Therefore, relying only on the information provided by seismic analyses might not be enough to create high-resolution fault reservoir models. However, analyzing seismic attributes can still be a good quality control of the facies spatial distributions obtained from outcrop compilations.

We demonstrate the potential of using seismic data for characterizing fault zone properties and its direct application for subsurface exploration. This study is in line with ongoing work on seismic interpretation of faults (Dutzer et al., 2010; Long and Imber, 2010, 2012; Iacopini et al., 2012, 2016; Botter et al., 2014, 2016, 2017; Torabi et al., 2016a, 2016b). By extracting seismic facies corresponding to the relative intensity of deformation within the fault zone, we are able to go a step further by defining facies probability trends for stochastic modeling. Despite some limitations regarding the fault facies model (e.g., uniform high-porosity sandstone and vertical fault) and the modeling method (e.g., computation of elastic properties and simplified ray-based seismic modeling), the results are promising and can be transferred with care to other studies. Future work will look at the application of this workflow (Figure 1) to reservoir models over production time (e.g., Fachri et al., 2016; Qu and Tveranger, 2016), more complex host rocks, fault configurations, different acquisition designs, and real seismic data.

Acknowledgments

This work was funded by the NORRUSS program of the Norwegian Research Council (NRC) through the SEISBARS project (grant no. 233646). Many ideas and methods applied in this paper are the result of the NRC project “Seismic imaging of fault zones” (grant no. 210425). D. Kolyukhin acknowledges support from the Russian Foundation for Basic Research (RFBR, grant

nos. 14-05-93090 and 15-55-20004). The fault facies model was done in RMS (Emerson) and Havana by D. Qu. We thank NORSAR for providing SeisRox where the seismic modeling was performed, and GeoTeric for providing SVI Plus where the seismic attribute analysis was done. We thank B. Alaei (Earth Science Analytics AS) for his help on the setup of seismic modeling. We thank G. A. Dorn, G. Yielding, two anonymous reviewers, and the associate editor for their insight and constructive feedback, which improved the manuscript.

References

- Antonellini, M., and A. Aydin, 1994, Effect of faulting on fluid flow in porous sandstones: Petrophysical properties: *AAPG Bulletin*, **78**, 355–377.
- Aydin, A., 1978, Small faults formed as deformation bands in sandstone: *Pure and Applied Geophysics PAGEOPH*, **116**, 913–930.
- Batzle, M., and Z. Wang, 1992, Seismic properties of pore fluids: *Geophysics*, **57**, 1396–1408.
- Botter, C., N. Cardozo, S. Hardy, I. Lecomte, and A. Escalona, 2014, From mechanical modeling to seismic imaging of faults: A synthetic workflow to study the impact of faults on seismic: *Marine and Petroleum Geology*, **57**, 187–207, doi: [10.1016/j.marpetgeo.2014.05.013](https://doi.org/10.1016/j.marpetgeo.2014.05.013).
- Botter, C., N. Cardozo, S. Hardy, I. Lecomte, G. Paton, and A. Escalona, 2016, Seismic characterization of fault damage in 3D using mechanical and seismic modeling: *Marine and Petroleum Geology*, **77**, 973–990, doi: [10.1016/j.marpetgeo.2016.08.002](https://doi.org/10.1016/j.marpetgeo.2016.08.002).
- Botter, C., N. Cardozo, I. Lecomte, A. Rotevatn, and G. Paton, 2017, The impact of faults and fluid flow on seismic images of a relay ramp over production time: *Petroleum Geoscience*, **23**, 17–28, doi: [10.1144/petgeo2016-027](https://doi.org/10.1144/petgeo2016-027).
- Braathen, A., J. Tveranger, H. Fossen, T. Skar, N. Cardozo, S. E. Semshaug, E. Bastesen, and E. Sverdrup, 2009, Fault facies and its application to sandstone reservoirs: *AAPG Bulletin*, **93**, 891–917, doi: [10.1306/03230908116](https://doi.org/10.1306/03230908116).
- Brogi, A., 2008, Fault zone architecture and permeability features in siliceous sedimentary rocks: Insights from the Rapolano geothermal area (Northern Apennines, Italy): *Journal of Structural Geology*, **30**, 237–256, doi: [10.1016/j.jsg.2007.10.004](https://doi.org/10.1016/j.jsg.2007.10.004).
- Caine, J. S., J. P. Evans, and C. B. Forster, 1996, Fault zone architecture and permeability structure: *Geology*, **24**, 1025–1028, doi: [10.1130/0091-7613\(1996\)024](https://doi.org/10.1130/0091-7613(1996)024).
- Chopra, S., and K. J. Marfurt, 2005, Seismic attributes — A historical perspective: *Geophysics*, **70**, no. 5, 3S0–2S0, doi: [10.1190/1.2098670](https://doi.org/10.1190/1.2098670).
- Chopra, S., and K. Marfurt, 2007, Seismic attributes for prospect identification and reservoir characterization: SEG, *Geophysical Developments Series* 11.
- Cohen, I., N. Coult, and A. A. Vassiliou, 2006, Detection and extraction of fault surfaces in 3D seismic data: *Geophysics*, **71**, no. 4, P21–P27, doi: [10.1190/1.2215357](https://doi.org/10.1190/1.2215357).
- Cressie, N. A. C., 1991, *Statistics for spatial data*: John Wiley & Sons, 920.
- Dumay, J., and F. Fournier, 1988, Multivariate statistical analyses applied to seismic facies recognition: *Geophysics*, **53**, 1151–1159, doi: [10.1190/1.1442554](https://doi.org/10.1190/1.1442554).
- Dutzer, J.-F., H. Basford, and S. Purves, 2010, Investigating fault-sealing potential through fault relative seismic volume analysis: *Petroleum Geology Conference Series*, **7**, 509–515.
- Fachri, M., A. Rotevatn, and J. Tveranger, 2013b, Fluid flow in relay zones revisited: towards an improved representation of small-scale structural Heterogeneities in flow models: *Marine and Petroleum Geology*, **46**, 144–164, doi: [10.1016/j.marpetgeo.2013.05.016](https://doi.org/10.1016/j.marpetgeo.2013.05.016).
- Fachri, M., J. Tveranger, A. Braathen, and P. Røe, 2016, Volumetric faults in field-sized reservoir simulation models: A first case study: *AAPG Bulletin*, **100**, 795–817, doi: [10.1306/02011614118](https://doi.org/10.1306/02011614118).
- Fachri, M., J. Tveranger, A. Braathen, and S. Schueller, 2013a, Sensitivity of fluid flow to deformation-band damage zone heterogeneities: A study using fault facies and truncated Gaussian simulation: *Journal of Structural Geology*, **52**, 60–79, doi: [10.1016/j.jsg.2013.04.005](https://doi.org/10.1016/j.jsg.2013.04.005).
- Fachri, M., J. Tveranger, N. Cardozo, and Ø. Pettersen, 2011, The impact of fault envelope structure on fluid flow: A screening study using fault facies: *AAPG Bulletin*, **95**, 619–648, doi: [10.1306/09131009132](https://doi.org/10.1306/09131009132).
- Faulkner, D. R., C. A. L. Jackson, R. J. Lunn, R. W. Schlische, Z. K. Shipton, C. A. J. Wibberley, and M. O. Withjack, 2010, A review of recent developments concerning the structure, mechanics and fluid flow properties of fault zones: *Journal of Structural Geology*, **32**, 1557–1575, doi: [10.1016/j.jsg.2010.06.009](https://doi.org/10.1016/j.jsg.2010.06.009).
- Fossen, H., and A. Bale, 2007, Deformation bands and their influence on fluid flow: *AAPG Bulletin*, **91**, 1685–1700, doi: [10.1306/07300706146](https://doi.org/10.1306/07300706146).
- Fossen, H., R. A. Schultz, Z. K. Shipton, and K. Mair, 2007, Deformation bands in sandstone: A review: *Journal of the Geological Society*, **164**, 755–769, doi: [10.1144/0016-76492006-036](https://doi.org/10.1144/0016-76492006-036).
- Fredman, N., J. Tveranger, N. Cardozo, A. Braathen, H. Soleng, P. Røe, A. Skorstad, and A. R. Yversveen, 2008, Fault facies modeling: Technique and approach for 3-D conditioning and modeling of faulted grids: *AAPG Bulletin*, **92**, 1457–1478, doi: [10.1306/06090807073](https://doi.org/10.1306/06090807073).
- Fredman, N., J. Tveranger, S. Semshaug, A. Braathen, and E. Sverdrup, 2007, Sensitivity of fluid flow to fault core architecture and petrophysical properties of fault rocks in siliciclastic reservoirs: A synthetic fault model study: *Petroleum Geoscience*, **13**, 305–320.
- Gassmann, F., 1951, Elasticity of porous media: *Vierteljahrsschrift der Naturforschenden Gesellschaft*, **96**, 1–23.
- Gersztenkorn, A., and K. J. Marfurt, 1999, Eigenstructure-based coherence computations as an aid to 3-D structural and stratigraphic mapping: *Geophysics*, **64**, 1468–1479, doi: [10.1190/1.1444651](https://doi.org/10.1190/1.1444651).
- Gringarten, E., and C. V. Deutsch, 2001, Teacher's aide variogram interpretation and modeling: *Mathematical Geology*, **33**, 507–534, doi: [10.1023/A:1011093014141](https://doi.org/10.1023/A:1011093014141).

- Hadley, G., 1969, *Elementary statistics*: Holden-Day, 457.
- Hald, A., 1952, *Statistical theory with engineering applications*: Wiley, 783.
- Hale, D., 2013, Methods to compute fault images, extract fault surfaces, and estimate fault throws from 3D seismic images: *Geophysics*, **78**, no. 2, O33–O43, doi: [10.1190/geo2012-0331.1](https://doi.org/10.1190/geo2012-0331.1).
- Horsrud, P., E. F. Sønstebo, and R. Bøe, 1998, Mechanical and petrophysical properties of North Sea shales: *International Journal of Rock Mechanics and Mining Sciences*, **35**, 1009–1020.
- Iacopini, D., and R. W. H. Butler, 2011, Imaging deformation in submarine thrust belts using seismic attributes: *Earth and Planetary Science Letters*, **302**, 414–422, doi: [10.1016/j.epsl.2010.12.041](https://doi.org/10.1016/j.epsl.2010.12.041).
- Iacopini, D., R. W. H. Butler, and S. Purves, 2012, Seismic imaging of thrust faults and structural damage: A visualization workflow for deepwater thrust belts: *First Break*, **30**, 77–84.
- Iacopini, D., R. W. H. Butler, S. Purves, N. McArdle, and N. De Freslon, 2016, Exploring the seismic expression of fault zones in 3D seismic volumes: *Journal of Structural Geology*, **89**, 54–73, doi: [10.1016/j.jsg.2016.05.005](https://doi.org/10.1016/j.jsg.2016.05.005).
- Koledoye, B. A., A. Aydin, and E. May, 2003, A new process-based methodology for analysis of shale smear along normal faults in the Niger Delta: *AAPG Bulletin*, **87**, 445–463.
- Kolyukhin, D., V. Lisitsa, D. Qu, M. Protasov, V. Tcheverda, J. Tveranger, and D. Vishnevsky, 2015, Seismic imaging of fault facies models: A pilot study: 4th International Conference on Fault and Top Seals 2015, EAGE, 95–99.
- Lecomte, I., 2008, Resolution and illumination analyses in PSDM: A ray-based approach: *The Leading Edge* (Tulsa, OK), **27**, 650–663, doi: [10.1190/1.2919581](https://doi.org/10.1190/1.2919581).
- Lecomte, I., P. L. Lavadera, I. Anell, S. J. Buckley, D. W. Schmid, and M. Heeremans, 2015, Ray-based seismic modeling of geologic models: Understanding and analyzing seismic images efficiently: *Interpretation*, **3**, no. 4, SAC71–SAC89.
- Lecomte, I., P. L. Lavadera, C. Botter, I. Anell, S. J. Buckley, C. H. Eide, A. Grippa, V. Mascolo, and G. Palladino, 2016, 2(3)D convolution modeling of complex geological targets beyond: 1D convolution: *First Break*, **34**, 99–107.
- Lisitsa, V., O. Podgornova, and V. Tcheverda, 2010, On the interface error analysis for finite difference wave simulation: *Computational Geosciences*, **14**, 769–778, doi: [10.1007/s10596-010-9187-1](https://doi.org/10.1007/s10596-010-9187-1).
- Long, J. J., and J. Imber, 2010, Geometrically coherent continuous deformation in the volume surrounding a seismically imaged normal fault-array: *Journal of Structural Geology*, **32**, 222–234, doi: [10.1016/j.jsg.2009.11.009](https://doi.org/10.1016/j.jsg.2009.11.009).
- Long, J. J., and J. Imber, 2012, Strain compatibility and fault linkage in relay zones on normal faults: *Journal of Structural Geology*, **36**, 16–26, doi: [10.1016/j.jsg.2011.12.013](https://doi.org/10.1016/j.jsg.2011.12.013).
- Manzocchi, T., C. Childs, and J. J. Walsh, 2010, Faults and fault properties in hydrocarbon flow models: *Geofluids*, **10**, 94–113, doi: [10.1111/j.1468-8123.2010.00283.x](https://doi.org/10.1111/j.1468-8123.2010.00283.x).
- Marfurt, K. J., and T. M. Alves, 2015, Pitfalls and limitations in seismic attribute interpretation of tectonic features: *Interpretation*, **3**, no. 1, SB5–SB15, doi: [10.1190/INT-2014-0122.1](https://doi.org/10.1190/INT-2014-0122.1).
- Mavko, G., T. Mukerji, and J. Dvorkin, 2009, *The rock physics handbook: Tools for seismic analysis of porous media*: Cambridge University Press, 329.
- Mitchum, R. M., Jr., P. R. Vail, and J. B. Sangree, 1977, Seismic stratigraphy and global changes of sea level. Part 6: Stratigraphic interpretations of seismic reflection patterns in depositional sequences, in C. E. Payton, ed., *Seismic stratigraphy: Applications to hydrocarbon exploration*: AAPG Memoir, 117–133.
- Nygård, R., M. Gutierrez, R. K. Bratli, and K. Høeg, 2006, Brittle-ductile transition, shear failure and leakage in shales and mudrocks: *Marine and Petroleum Geology*, **23**, 201–212, doi: [10.1016/j.marpetgeo.2005.10.001](https://doi.org/10.1016/j.marpetgeo.2005.10.001).
- Pei, Y., D. A. Paton, R. J. Knipe, and K. Wu, 2015, A review of fault sealing behaviour and its evaluation in siliciclastic rocks: *Earth-Science Reviews*, **150**, 121–138, doi: [10.1016/j.earscirev.2015.07.011](https://doi.org/10.1016/j.earscirev.2015.07.011).
- Qu, D., P. Røe, and J. Tveranger, 2015, A method for generating volumetric fault zone grids for pillar gridded reservoir models: *Computers & Geosciences*, **81**, 28–37, doi: [10.1016/j.cageo.2015.04.009](https://doi.org/10.1016/j.cageo.2015.04.009).
- Qu, D., and J. Tveranger, 2016, Incorporation of deformation band fault damage zones in reservoir models: *AAPG Bulletin*, **100**, 423–443, doi: [10.1306/12111514166](https://doi.org/10.1306/12111514166).
- Qu, D., J. Tveranger, and M. Fachri, 2017, Influence of deformation-band fault damage zone on reservoir performance: *Interpretation*, **5**, this issue, doi: [10.1190/int-2016-0229.1](https://doi.org/10.1190/int-2016-0229.1).
- Rotevatn, A., H. Fossen, J. Hesthammer, T. E. Aas, and J. A. Howell, 2007, Are relay ramps conduits for fluid flow? Structural analysis of a relay ramp in Arches National Park, Utah, in L. Lonergan, D. J. Sanderson, R. J. H. Jolly, and K. Rawnsley, eds., *Fractured reservoirs: Geological Society of London, Special Publication*, 55–71.
- Schueller, S., A. Braathen, H. Fossen, and J. Tveranger, 2013, Spatial distribution of deformation bands in damage zones of extensional faults in porous sandstones: Statistical analysis of field data: *Journal of Structural Geology*, **52**, 148–162, doi: [10.1016/j.jsg.2013.03.013](https://doi.org/10.1016/j.jsg.2013.03.013).
- Sheriff, R. E., and L. P. Geldart, 1995, *Exploration seismology*: Cambridge University Press.
- Soleng, H. H., A. R. Syversveen, A. Skorstad, P. Roe, and J. Tveranger, 2007, Flow through inhomogeneous fault zones: Presented at the SPE Annual Technical Conference and Exhibition, doi: [10.2118/110331-MS](https://doi.org/10.2118/110331-MS).
- Syversveen, A. R., A. H. Skorstad, H. Soleng, P. Røe, and J. Tveranger, 2006, Facies modelling in fault zones: ECMOR X — 10th European Conference on the Mathematics of Oil Recovery, doi: [10.3997/2214-4609.201402485](https://doi.org/10.3997/2214-4609.201402485).

- Taner, M., 2001, Seismic attributes: CSEG Recorder, **26**, 48–56.
- Taner, M. T., F. Koehler, and R. E. Sheriff, 1979, Complex seismic trace analysis: *Geophysics*, **44**, 1041–1063, doi: [10.1190/1.1440994](https://doi.org/10.1190/1.1440994).
- Torabi, A., B. Alaei, and D. Kolyukhin, 2016a, Analysis of fault scaling relations using fault seismic attributes: *Geophysical Prospecting*, **65**, 581–595, doi: [10.1111/1365-2478.12440](https://doi.org/10.1111/1365-2478.12440).
- Torabi, A., B. Alaei, D. Kolyukhin, R. H. Libak, R. H. Gabrielsen, and A. Braathen, 2016b, Fault geometric and seismic attributes: An integrated study with focus on the Barents Sea: *First Break*, **34**, 73–80.
- Torabi, A., H. Fossen, and A. Braathen, 2013, Insight into petrophysical properties of deformed sandstone reservoirs: *AAPG Bulletin*, **97**, 619–637, doi: [10.1306/10031212040](https://doi.org/10.1306/10031212040).
- Townsend, C., I. R. Firth, R. Westerman, L. Kirkevollen, M. Hårde, and T. Andersen, 1998, Small seismic-scale fault identification and mapping, in G. Jones, Q. J. Fisher, and R. J. Knipe, eds., *Faulting, fault sealing and fluid flow in hydrocarbon reservoirs*: Geological Society of London, Special Publications, 1–25.
- Tveranger, J., A. Braathen, T. Skar, and A. Skaug, 2005, Centre for integrated petroleum research: Research activities with emphasis on fluid flow in fault zones: *Norwegian Journal of Geology*, **85**, 63–71.
- Vail, P. R., 1987, Seismic stratigraphy interpretation using sequence stratigraphy: Part 1: Seismic stratigraphy interpretation procedure, in A. W. Bally, ed., *Atlas of Seismic Stratigraphy*, vol. 1: AAPG Studies in Geology 27, 1–10.
- Virieux, J., 1986, P-SV wave propagation in heterogeneous media: Velocity-stress finite-difference method: *Geophysics*, **51**, 889–901, doi: [10.1190/1.1442147](https://doi.org/10.1190/1.1442147).
- Vishnevsky, D. M., D. R. Kolyukhin, D. Qu, V. V. Lisitsa, M. I. Protasov, J. Tveranger, and V. A. Tcheverda, 2014, Statistical analysis of seismic images of a fault facies model: *Seismic Technology*, **11**, 1–11, doi: [10.3997/2405-7495.2015109](https://doi.org/10.3997/2405-7495.2015109).
- Wibberley, C. A. J., G. Yielding, and G. Di Toro, 2008, Recent advances in the understanding of fault zone internal structure: A review, in C. A. J. Wibberley, W. Kurz, J. Imber, R. E. Holdsworth, and C. Collettini, eds., *The internal structure of fault zones: Implications for mechanical and fluid-flow properties*: Geological Society of London, Special Publications, 5–33.
- Wood, A. M., D. A. Paton, and R. E. L. L. Collier, 2015, The missing complexity in seismically imaged normal faults: What are the implications for geometry and production response? in F. L. Richards, N. J. Richardson, S. J. Ripington, R. W. Wilson, and C. E. Bond, eds., *Industrial structural geology: Principles, techniques and integration*: Geological Society of London, Special Publications, 213–230.



Charlotte Botter received a Ph.D. (2016) in petroleum geosciences from the University of Stavanger, Norway. She is a postdoctoral researcher in the geophysics section of the Dublin Institute of Advanced Studies, Ireland. Her research interests include numerical modeling of geologic processes, faulting, and seismic characterization.



Nestor Cardozo received a Ph.D. in geology from Cornell University. He is a professor in the Department of Petroleum Engineering, University of Stavanger. He teaches undergraduate and graduate courses in structural geology and its application to petroleum geosciences. He has also developed several computer programs for structural geology and basin modeling. His research interests include faults and their related deformation, including seismic imaging, interpretation, and modeling of these structures.



Dongfang Qu received a B.S. (2008) in petroleum geology from the China University of Petroleum and a Ph.D. (2015) from the Department of Earth Science, University of Bergen, Norway. Her research interests include geomodeling, faults, and fluid flow.



Jan Tveranger received a Dr. Scient. (1995) from the University of Bergen. Prior work postings include positions at the Department of Earth Sciences, University of Bergen, Saga Petroleum, and Norsk Hydro. He is a senior researcher at Uni Research CIPR in Bergen, Norway. His research interests include geomodeling, sedimentology, and structural geology.



Dmitriy Kolyukhin received an M.S. (1998) from the Novosibirsk State University and a Ph.D. (2005) from the Institute of Computational Mathematics and Mathematical Geophysics SB RAS. He is a senior researcher at the Trofimuk Institute of Petroleum Geology and Geophysics SB RAS. His scientific research interests include statistical modeling, geostatistics, Monte Carlo methods, fault modeling, reservoir characterization, and fluid flow in fractured reservoirs.